Anomalous Hall effect in a compensated ferrimagnet: Symmetry analysis for Mn_3Al

Minkyu Park [1,2] Guihyun Han [2] and S. H. Rhim [2,*]

[1]*Research Institute of Basic Sciences, University of Ulsan, 93, Daehak-ro, Nam-gu, Ulsan 44610, Republic of Korea*

[2]*Department of Physics, University of Ulsan, 93, Daehak-ro, Nam-gu, Ulsan 44610, Republic of Korea*

(Received 12 April 2021; revised 21 February 2022; accepted 24 February 2022; published 22 March 2022)

It has long been believed that the anomalous Hall effect (AHE) can only be observed in ferromagnets. However, any magnetic material can exhibit AHE due to the broken time-reversal symmetry. In this work, we present a nontrivial AHE on the compensated ferrimagnet Mn_3Al using symmetry arguments and first-principles calculations. Nonzero components of anomalous Hall conductivity $\sigma_{\alpha\beta}$ are determined based on the magnetic space group of Mn_3Al. The explicit first-principles calculation confirms $\sigma_{xy} = -320\ (\Omega\,\mathrm{cm})^{-1}$. The nature of Berry curvature responsible for the intrinsic origin of AHE is further identified using group theory: lifted degeneracies at $\frac{1}{2}K\Gamma$, L, and $\frac{1}{2}K'\Gamma$ induced by spin-orbit interactions. Moreover, the global behaviors of Berry curvatures are shown over the whole Brillouin zone which reveal the overlooked contributions around X'.

DOI: 10.1103/PhysRevResearch.4.013215

I. ANOMALOUS HALL EFFECT

Ever since the discovery of the anomalous Hall effect (AHE), virtually all studies have been focused on ferromagnets. For ferromagnets, the intrinsic origin of AHE was initially pioneered by Karplus and Luttinger [1], where the spin-orbit interaction (SOI) is supposed to be proportional to the net magnetization. Although this assumption is only valid in ferromagnets, it has been believed that AHE necessarily accompanies a net magnetization.

The modern understanding of AHE employs the Berry curvature, which characterizes the topological nature of electronic structures [2]. Apart from the extrinsic contributions due to impurities, the intrinsic anomalous Hall conductivity (AHC) is derived from the linear response theory (or from Kubo formula) as

$$\sigma_{\alpha\beta} = \frac{e^2}{\hbar}\int_{\mathrm{BZ}}\frac{d^3k}{(2\pi)^3}\sum_n f(\epsilon_{n\mathbf{k}})\Omega_{n,\alpha\beta}(\mathbf{k}), \tag{1}$$

where $\Omega_{n,\alpha\beta}(\mathbf{k})$ is the Berry curvature of the nth band and $f(\epsilon_{n\mathbf{k}})$ is the Fermi-Dirac distribution function; the integration is performed over the Brillouin zone (BZ). The Berry curvature is defined in terms of the Berry connection $A_{n,\alpha}(\mathbf{k}) = -i\langle u_{n\mathbf{k}}|\partial_\alpha|u_{n\mathbf{k}}\rangle$ as $\Omega_{n,\alpha\beta}(\mathbf{k}) = \partial_\alpha A_{n,\beta}(\mathbf{k}) - \partial_\beta A_{n,\alpha}(\mathbf{k})$ where the derivatives are taken with respect to the crystal momentum $\mathbf{k}$. Here $|u_{n\mathbf{k}}\rangle$ represents the periodic part of the nth Bloch state.

Clearly from Eq. (1), AHC vanishes in a time-reversal (TR) symmetric system because the Berry curvature is odd under the TR T, i.e., $T : \Omega_{n,\alpha\beta}(\mathbf{k}) \to -\Omega_{n,\alpha\beta}(-\mathbf{k})$. Therefore AHE can only arise in the *absence* of the TR symmetry, namely, in *any* magnetic material [3].

Other symmetries can further constrain the form of AHC [4,5]. For example, in bipartite antiferromagnets, AHC vanishes due to the antitranslation which is the composite symmetry of the TR and the translation between two sublattices. This is why such simple antiferromagnets do *not* exhibit AHE. However, if such symmetries, which let AHC vanish, are absent, nontrivial AHE can exist. Indeed, recent studies on antiferromagnets [6–17] and a compensated ferrimagnet [18] have revealed that a nontrivial AHC can exist without a net magnetization [19].

In this work, we confirm that the net magnetization is *not* essential for AHE by investigating a compensated collinear ferrimagnet Mn_3Al [20–22]. More specifically, we identify the magnetic space group of Mn_3Al and discuss its constraints on AHC. We further analyze how and why the Berry curvature arises at some specific regions in BZ based on group theory. Moreover, the global features of Berry curvature are revealed over whole BZ. Finally, AHC is explicitly evaluated to confirm expected features.

II. CRYSTAL STRUCTURE AND MAGNETIC SYMMETRY

Mn_3Al, a regular Heusler compound, has the structure shown in Fig. 1 with the space group $Fm\bar{3}m$ (No. 225). It is a face-centered cubic (fcc) structure with lattice constant $a = 5.80$ Å [20–22]. Two inequivalent Mn sites are distinguished by Mn(I) and Mn(II), depending on the site symmetry. Both Al and Mn(I) take fcc sites with the relative translation by $(\frac{1}{2}, \frac{1}{2}, \frac{1}{2})$ in lattice coordinates. Mn(II) can be viewed as insertions to the center of cubes formed by Al and Mn(I). Table I lists structural information such as Wyckoff positions, site symmetries, and magnetic moments.

As will be demonstrated from first-principles calculations, Mn_3Al stabilizes in a collinear ferrimagnetic phase. The

*sonny@ulsan.ac.kr

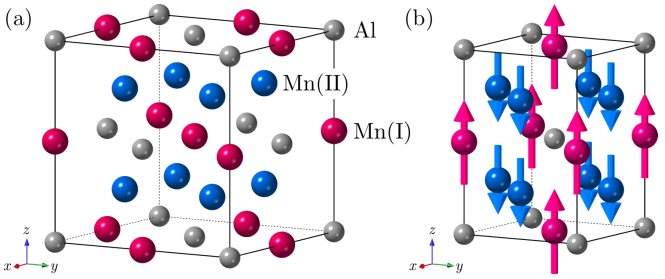

FIG. 1. (a) Structure of Mn_3Al in conventional cubic unit cell with space group $Fm\bar{3}m$ (No. 225). (b) Magnetic unit cell in the presence of magnetic moments, denoted by arrows, along the z axis, whose magnetic space group is $I4/mm'm'$ (No. 139.537).

choice of the magnetization axis along the z axis, as depicted in Fig. 1(b), alters the governing symmetry from cubic to tetragonal. As a result, the symmetry is described by the magnetic space group $I4/mm'm'$ (No. 139.537) [23], where the prime denotes the TR [24–28]. $I4/mm'm'$, which does not include antitranslations, contains the principal fourfold rotation 4_{001}; twofold rotations $2'_{100}$ and $2'_{1\bar{1}0}$; and inversion $\bar{1}$ as well as mirror planes perpendicular to the rotation axes, m_{001}, m'_{100}, and $m'_{1\bar{1}0}$. We remind one here that $I4/mm'm'$ is the same magnetic space group of the body-centered cubic iron with the magnetization along the z axis [23].

Now we discuss the constraints imposed on AHC $\sigma_{\alpha\beta} = (\sigma_{yz}, \sigma_{zx}, \sigma_{xy})$ by $I4/mm'm'$. For AHC, the magnetic point group $4/mm'm'$ suffices to determine the constraints [4,5]. From the transformation rules of $\sigma_{\alpha\beta}$ which is a pseudovector, we can obtain all constraints. For example, for twofold rotation, $2_{001} : (\sigma_{yz}, \sigma_{zx}, \sigma_{xy}) \to (-\sigma_{yz}, -\sigma_{zx}, \sigma_{xy})$, which results in $\sigma_{yz} = \sigma_{zx} = 0$. Furthermore, no symmetry operation makes σ_{xy} vanish because the z component of a pseudovector is invariant under any operation of $4/mm'm'$ [26–28]. Consequently, $I4/mm'm'$ allows only σ_{xy} to be nontrivial:

$$\sigma_{\alpha\beta} = (0, 0, \sigma_{xy}). \tag{2}$$

Similarly, we can perform the symmetry analysis for any given system. For this purpose, we summarize how a certain type of symmetry operation constrains AHC in Table II of Appendix A.

TABLE I. Structural information of Mn_3Al, whose space group is $Fm\bar{3}m$ (No. 225); atomic positions of representative atoms along with Wyckoff positions and their site symmetry are in lattice coordinates of the conventional cubic unit cell as shown in Fig. 1(a). Magnetic moments are in units of μ_B.

Atom	Wyckoff position	Site symmetry	x	y	z	m_z
Al	4a	$m\bar{3}m$ (O_h)	0	0	0	0.01
Mn(I)	4b	$m\bar{3}m$ (O_h)	$\frac{1}{2}$	$\frac{1}{2}$	$\frac{1}{2}$	2.72
Mn(II)	8c	$\bar{4}3m$ (T_d)	$\frac{1}{4}$	$\frac{1}{4}$	$\frac{1}{4}$	−1.36
			$\frac{1}{4}$	$\frac{1}{4}$	$\frac{3}{4}$	

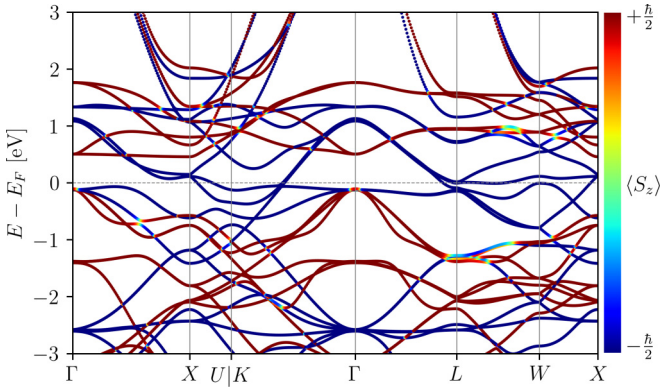

FIG. 2. Band structures along the high-symmetry lines of the fcc lattice. Colors represent $\langle S_z \rangle$. Half-metallicity is evident with gap in the spin-up bands. Fermi energy E_F is set to zero.

III. COMPUTATIONAL METHODS

Electronic structure calculations are performed using the QUANTUM ESPRESSO package [29,30]. Generalized gradient approximation is employed based on Perdew-Burke-Ernzerhof parametrization [31] within projector augmented wave basis [32]. SOI is included in the scheme of fully relativistic pseudopotentials from PSlibrary [33]. The valence electron configuration for Al is [Ne]$3s^2 3p^1$ and for Mn is [Ar]$3d^5 4s^2$ with semicore $3s$ and $3p$ states. Cutoffs for wave function and charge density expansions are 67 Ry and 344 Ry, respectively. For the self-consistent calculation, a $19 \times 19 \times 19$ Monkhorst-Pack grid [34] is used.

After the self-consistent calculation, maximally localized Wannier functions are constructed using the WANNIER90 package [35], where a $9 \times 9 \times 9$ k grid is used for non-self-consistent calculation. The validity of Wannier functions is examined using the POSTW90 code in WANNIER90 by comparing the band structure from QUANTUM ESPRESSO. The Berry curvature is computed both by POSTW90 and WANNIERBERRI [36]; the former for plotting along high-symmetry lines, while the latter for plotting in the whole BZ. AHC is then explicitly evaluated using WANNIERBERRI with a $600 \times 600 \times 600$ k grid and double-checked by POSTW90 with a coarser grid only at the Fermi energy.

IV. RESULTS AND DISCUSSIONS

A. Band structures and Berry curvature

First-principles calculations confirm that Mn_3Al exhibits a compensated collinear ferrimagnetism consistent with previous studies [20–22]. Magnetic moments of individual atoms are listed in Table I, where vanishing total magnetization is evident.

Band structures along high-symmetry lines are shown in Fig. 2. As spin is not a good quantum number with SOI, $\langle S_z \rangle$ is presented instead. Most bands are well characterized by $\langle S_z \rangle$ except some regions which do not affect our discussion. The half-metallicity is evident with gap in the spin-up bands. Our result is consistent with calculations using WIEN2K without SOI [21].

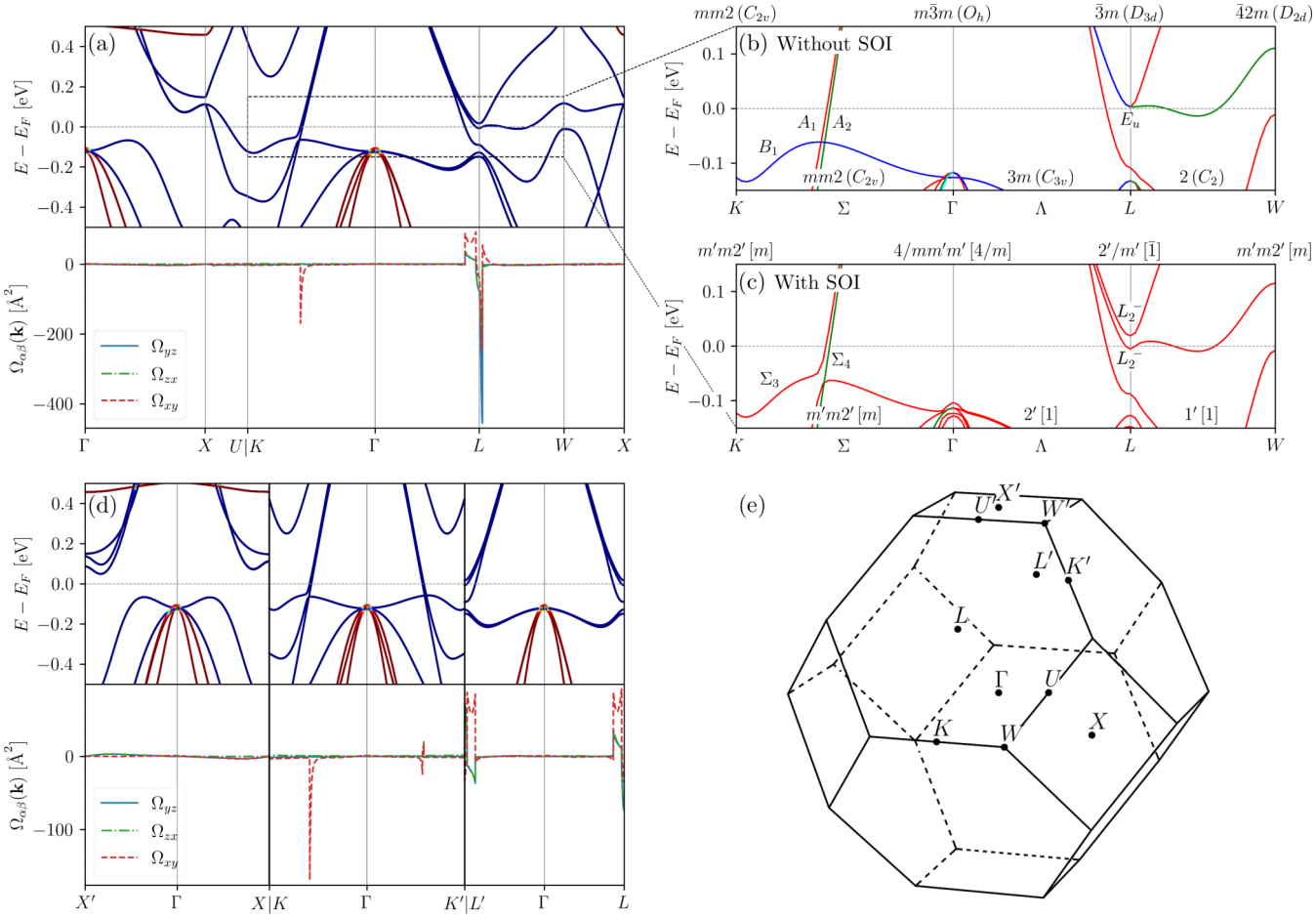

FIG. 3. (a) Band structures in a narrow energy window and Berry curvature $\Omega_{\alpha\beta}(\mathbf{k})$ along the same path as in Fig. 2. (b),(c) Band structures in the vicinity of E_F (b) without and (c) with SOI. Reduced symmetry due to SOI induces a finite Berry curvature. Little groups of high-symmetry points (lines) are shown at the top (bottom) of each figure. The irreps of bands at L and Σ are denoted where different irreps are distinguished by colors. In (c), the unitary subgroup of the little group is shown in square brackets. (d) Band structures and Berry curvature along X'-Γ-X, K-Γ-K', and L'-Γ-L to illustrate broken cubic symmetry due to SOI. (e) Labels of high-symmetry points in the Brillouin zone.

Before we get into details on Berry curvatures, we remind one that the Berry curvature originates from band mixing through interactions in which SOI is a prominent example. Moreover, in magnetic materials, SOI breaks part of the crystal symmetry. So the degeneracies protected by those symmetries are lifted and large Berry curvatures can emerge there. As shown below, this is observed in both an *accidental* degeneracy such as a nodal line protected by a mirror-reflection symmetry and an *essential* degeneracy protected by a little group, or group of $\mathbf{k}$ [37].

In Fig. 3(a), we show the *total* Berry curvatures $\Omega_{\alpha\beta}(\mathbf{k}) = \sum_n f(\epsilon_{n\mathbf{k}})\Omega_{n,\alpha\beta}(\mathbf{k})$ along the same high-symmetry lines as in Fig. 2. As seen, pronounced features are well manifested around $\frac{1}{2}K\Gamma$ and L. As just explained, the origin of Berry curvatures can be understood based on the reduced symmetry due to SOI. Hence, we present band structures in the vicinity of E_F in Figs. 3(b) and 3(c) without and with SOI, respectively. By comparing Figs. 3(b) and 3(c), we observe (i) two bands around $\frac{1}{2}K\Gamma$ are mixed and (ii) a degenerate band along Λ connecting Γ and L is lifted. This is further analyzed in detail based on the little groups. In the following analysis, the ordinary point groups are adopted as little groups in the absence of SOI, whereas the magnetic point groups are used in the presence of SOI.

Let us first focus on $\frac{1}{2}K\Gamma$. In the absence of SOI, the little group of Σ connecting K and Γ is $mm2\,(C_{2v})$. As denoted in Fig. 3(b), three bands below E_F belong to three one-dimensional (1D) irreducible representations (irreps), A_1, A_2, and B_1. By turning on SOI, the little group changes to $m'm2'$ and each band now belongs to one of two 1D irreps, Σ_3 and Σ_4 of $m'm2'$ [38]. As a consequence, two bands belonging to Σ_3 exhibit a level repulsion which induces large Berry curvatures. But why does only $\Omega_{xy}(\mathbf{k})$ have nonzero value along Σ? The mirror-reflection symmetry m_{001} is the key. Under m_{001}, $\Omega_{\alpha\beta}(\mathbf{k})$ transforms as $m_{001} : (\Omega_{yz}, \Omega_{zx}, \Omega_{xy})(\mathbf{k}) \to (-\Omega_{yz}, -\Omega_{zx}, \Omega_{xy})(k_x, k_y, -k_z)$. Thus, only $\Omega_{xy}(\mathbf{k})$ can be nontrivial in the mirror-invariant plane $k_z = 0$ that includes Σ.

The Berry curvatures at $\frac{1}{2}K\Gamma$ can instead be understood in terms of a gapped nodal line [39–42] which is a lifted accidental degeneracy. As is well known, if two bands with different mirror eigenvalues cross, a nodal line exists in the mirror-invariant plane. In our case, the band crossing in Fig. 3(b) between A_1 and B_1 was protected by the mirror-reflection

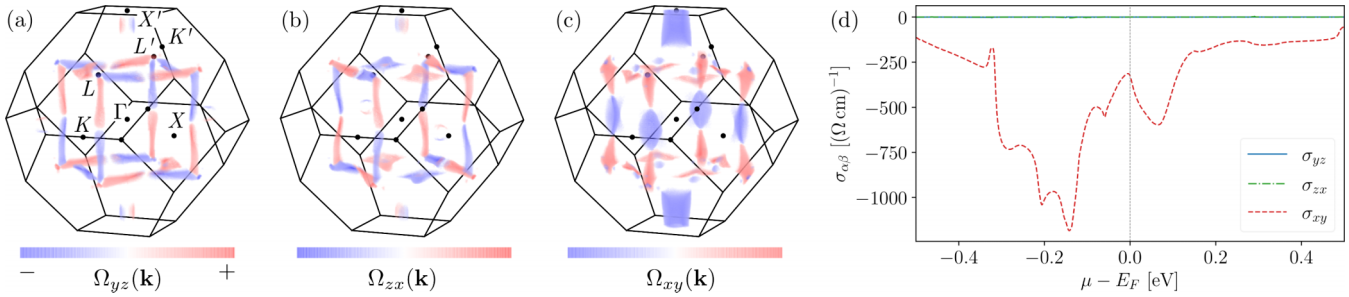

FIG. 4. (a)–(c) Each component of total Berry curvature, $\Omega_{\alpha\beta}(\mathbf{k}) = \sum_n f(\epsilon_{n\mathbf{k}})\Omega_{n,\alpha\beta}(\mathbf{k})$, plotted in the whole BZ. The difference between X and X' is prominent in (c): Berry curvatures obey the tetragonal symmetry $I4/mm'm'$ instead of the cubic symmetry $Fm\bar{3}m$. For better visibility, the logarithmic scale $f(x) = \mathrm{sgn}(x)\log_{10}(1+|x|)$ is used, where $|\Omega_{\alpha\beta}(\mathbf{k})| \leqslant 10$ Å^2 are excluded. The maximum and minimum values are set to $\pm|f(x_0)|$ with $x_0 = \max|\Omega_{\alpha\beta}(\mathbf{k})|$. (d) AHC $\sigma_{\alpha\beta}$ as a function of the chemical potential μ. As required by the symmetry, $\sigma_{yz} = \sigma_{zx} = 0$ at any μ. At $\mu = E_F$, $\sigma_{xy} = -320$ $(\Omega\,\mathrm{cm})^{-1}$.

symmetry $m_{1\bar{1}0}$ while that between A_2 and B_1 was by m_{001}. The former symmetry $m_{1\bar{1}0}$ is broken by SOI and large Berry curvatures around the gapped nodal line are induced.

Let us now turn to L. Without SOI, the degenerate band just above E_F belongs to the two-dimensional (2D) irrep E_u of $\bar{3}m$ (D_{3d}). By turning on SOI, the degeneracy is lifted and each band belongs to the 1D irrep L_2^- of the little group $2'/m'$ with one above E_F and the other below. This leads to large Berry curvatures at L. The Berry curvatures along Λ can be understood similarly because the only difference is the inversion symmetry $\bar{1}$.

Note that the nature of the origin of Berry curvatures around L is different from that of $\frac{1}{2}K\Gamma$. While the former is originated from lifted essential degeneracy, the latter is from lifted accidental degeneracy.

We emphasize that nonzero $\Omega_{\alpha\beta}(\mathbf{k})$ at some high-symmetry points or lines does not necessarily imply a nontrivial AHC. To estimate AHC qualitatively, we need to extend the Berry curvature in Fig. 3(a) to whole BZ. In doing so, one should be careful about the use of the symmetry, because the magnetism breaks some crystal symmetry. This is illustrated in Fig. 3(d) along three different paths X'-Γ-X, K-Γ-K', and L'-Γ-L where high-symmetry points are denoted in Fig. 3(e).

For each segment of the paths in Fig. 3(d), we observe the following. (i) X'-Γ-X: Band structures are slightly asymmetric because 4_{100} is broken in the presence of the magnetism. The Berry curvature shows no meaningful difference. (ii) K-Γ-K': A significant difference in Berry curvature originates from the different behavior of band mixing around $\frac{1}{2}K\Gamma$ and $\frac{1}{2}K'\Gamma$. Around $\frac{1}{2}K'\Gamma$, both band crossings, or nodal lines, shown in Fig. 3(b) are gapped in the presence of SOI. (iii) L'-Γ-L: Band structures are symmetric because L and L' are connected by 2_{001}. The Berry curvature is symmetric for $\Omega_{xy}(\mathbf{k})$ and antisymmetric for $\Omega_{yz}(\mathbf{k})$ and $\Omega_{zx}(\mathbf{k})$. Thus, the contributions to σ_{yz} and σ_{zx} from the neighborhood of L and its equivalents cancel among them regardless of the value of Berry curvature.

B. Anomalous Hall conductivity

As mentioned, the integration of total Berry curvature over BZ gives AHC. We show the total Berry curvatures in the whole BZ in Figs. 4(a)–4(c) where the above analysis becomes more evident. Notably, almost all contributions reside around the edges of the cube formed by L and its equivalents with exceptions around X' and $-X'$. The negative contributions of $\Omega_{xy}(\mathbf{k})$ around X' is a shape of a hollow cylinder which is compatible with Fig. 3(d). In Appendix B, the origin of Berry curvatures around X' is discussed in terms of the lifted essential degeneracy due to SOI.

It is worth emphasizing that the contributions around X' cannot be captured by the conventional high-symmetry lines of fcc lattices where X and X' are treated equivalently. However, the k path of the body-centered tetragonal lattice, taking account of the magnetic space group, can capture the inequivalence of X and X'.

From this global behavior of Berry curvature, all symmetry constraints can be visually verified. More specifically, the relation $\Omega_{yz}(\mathbf{k}) = -\Omega_{zx}(k_y, -k_x, k_z)$ required by 4_{001} is easily confirmed from Figs. 4(a) and 4(b). The mirror-reflection symmetry m_{001} is also evident for all components. Moreover, $\Omega_{xy}(\mathbf{k})$ is invariant under all symmetry operations of $I4/mm'm'$ which is compatible with Eq. (2).

In Fig. 4(d), we show $\sigma_{\alpha\beta}$ as a function of the chemical potential μ. Note that σ_{xy} at $\mu = E_F$, which is obtained by adding all contributions of total Berry curvature shown in Fig. 4(c), sits at a local maximum. Hence, the positive $\Omega_{xy}(\mathbf{k})$ around L and $\frac{1}{2}K'\Gamma$ are quite comparable to the negative $\Omega_{xy}(\mathbf{k})$ around $\frac{1}{2}K\Gamma$ and X'. As seen, only σ_{xy} survives with -320 $(\Omega\,\mathrm{cm})^{-1}$ at $\mu = E_F$, while other components, σ_{yz} and σ_{zx}, vanish with respect to μ as required by the symmetry. Moreover, σ_{xy} reaches -1200 and -600 $(\Omega\,\mathrm{cm})^{-1}$ for $\mu - E_F \approx -0.14$ and 0.07 eV, respectively.

C. Anomalous Nernst conductivity

Anomalous Nernst effect, closely related to AHE, is a phenomenon that a current is induced by a temperature gradient, $J_\alpha = \alpha_{\alpha\beta}(-\partial_\beta T)$, where J_α is the current density, $\alpha_{\alpha\beta}$ is the anomalous Nernst conductivity (ANC), and T is temperature. At low temperature, ANC is expressed by the Mott relation [43]

$$\alpha_{\alpha\beta} = \frac{\pi^2}{3}\frac{k_B^2 T}{e}\lim_{T\to 0}\frac{\partial\sigma_{\alpha\beta}}{\partial\mu}, \tag{3}$$

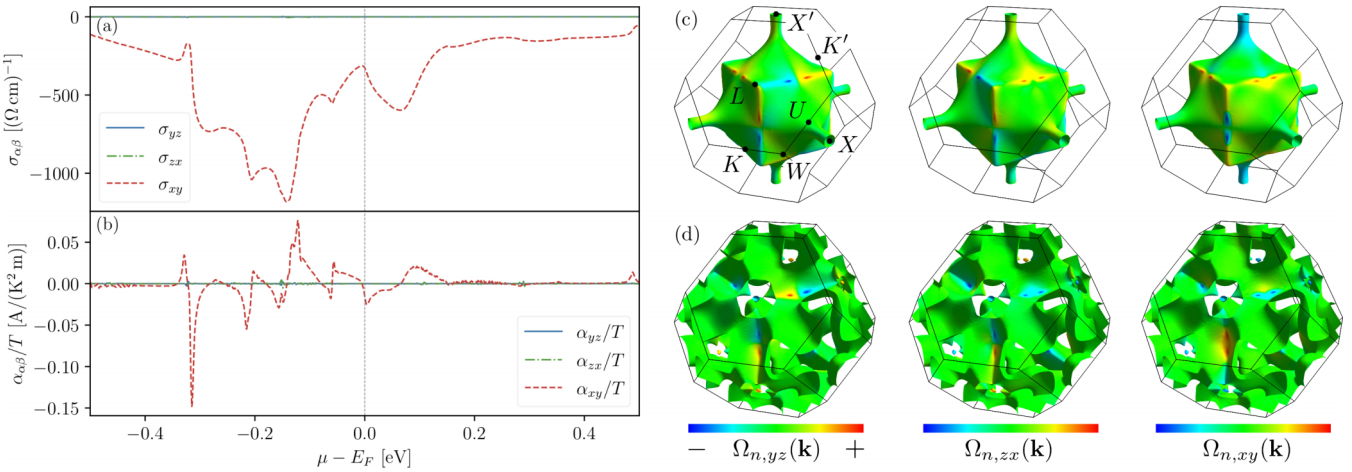

FIG. 5. (a) AHC $\sigma_{\alpha\beta}$ and (b) ANC $\alpha_{\alpha\beta}$ divided by T as a function of the chemical potential μ. At $\mu = E_F$, $\alpha_{xy}/T = -0.015$ A/(K² m). (c),(d) The Berry curvature $\Omega_{n,\alpha\beta}(\mathbf{k})$ on the Fermi surface: (c) hole- and (d) electronlike sheets of the Fermi surface. The logarithmic scale, $f(x) = \mathrm{sgn}(x)\log_{10}(1 + |x|)$, is used for better visibility. The maximum and minimum values are set to $\pm|f(x_0)|$ with $x_0 = \max|\Omega_{n,\alpha\beta}(\mathbf{k})|$.

where k_B is the Boltzmann constant. Hence, ANC can be obtained by taking the derivative of AHC. In Fig. 5(b), ANC divided by T is shown as a function of the chemical potential μ. At $\mu = E_F$, $\alpha_{xy}/T = -0.015$ A/(K² m) and it reaches as large as -0.15 A/(K² m) when $\mu - E_F \approx -0.32$ eV. Note that ANC obeys the same symmetry constraints of AHC.

The explicit expression of $\partial\sigma_{\alpha\beta}/\partial\mu$ at low temperatures is given as [43]

$$\lim_{T\to 0}\frac{\partial\sigma_{\alpha\beta}}{\partial\mu} = \frac{e^2}{\hbar}\int_{\mathrm{BZ}}\frac{d^3k}{(2\pi)^3}\sum_n \delta(E_F - \epsilon_{n\mathbf{k}})\Omega_{n,\alpha\beta}(\mathbf{k}), \quad (4)$$

which implies that what is responsible for ANC is the sum of Berry curvature on the *Fermi surface*, whereas the sum of Berry curvature of *occupied states* is for AHC.

Based on Eq. (4), we can alternatively evaluate ANC by summing Berry curvature on the Fermi surface. To give more insight, Berry curvature is plotted on the Fermi surface in Figs. 5(c) and 5(d) using FermiSurfer [44]. The large $\Omega_{n,\alpha\beta}(\mathbf{k})$ is from two regions: (i) from the vicinity of $\frac{1}{2}K\Gamma$ and $\frac{1}{2}K'\Gamma$; and (ii) from the neck along the X' of the holelike sheet [Fig. 5(c)] and the small pocket of the electronlike sheet near L [Fig. 5(d)]. In the former, the contributions from the electron- and hole-like sheets seem to cancel out. In the latter, only $\Omega_{n,xy}(\mathbf{k})$ seems to give the net contributions of ANC. Note that the presence of $\Omega_{n,xy}(\mathbf{k})$ along X' and the absence along X in Fig. 5(c) indicates broken cubic symmetry due to magnetism.

V. CONCLUSIONS

In conclusion, the nontrivial AHE has been presented in the collinear ferrimagnet Mn_3Al with zero net magnetization. The analysis of symmetry constraints on AHC under the magnetic space group $I4/mm'm'$ shows that only σ_{xy} can survive. To demonstrate our reasoning, we have calculated Berry curvatures and AHC using first-principles calculations. The large Berry curvatures have been observed around $\frac{1}{2}K\Gamma$, L, $\frac{1}{2}K'\Gamma$, and X' whose origins have been classified into two types: lifted accidental and essential degeneracies. The nature of the origin of Berry curvatures has been coherently explained using group theory. We have also emphasized that both types of lifted degeneracy are equally important for AHE regardless of the type. Finally, the explicit calculation of AHC shows $\sigma_{xy} = -320\ (\Omega\,\mathrm{cm})^{-1}$ at the Fermi energy, which becomes as large as $-1200\ (\Omega\,\mathrm{cm})^{-1}$ with hole doping.

ACKNOWLEDGMENTS

This work was supported by the National Research Foundation of Korea (NRF) grant funded by the Korea government (MSIT) (Grant No. NRF-2019R1I1A3A01059880).

APPENDIX A: SYMMETRY CONSTRAINTS ON ANOMALOUS HALL CONDUCTIVITY

In general, the symmetry constrains the form of physical quantities. For AHC, magnetic point groups are enough to discuss constraints imposed by the symmetry [4,5]. Although the correspondence between magnetic point groups and allowed components of AHC is given in the literature, we summarize it in a slightly different way in Table II for our convenience.

To obtain Table II, we note that for any symmetry operation in a magnetic point group, AHC, which is a pseudovector and

TABLE II. Symmetry constraints imposed on $\sigma_{\alpha\beta}$. The symmetry axis is taken along the z axis, i.e., $\mathbf{n} = \hat{z}$. The prime denotes TR and $n \in \{2, 3, 4, 6\}$.

Proper rotation	Improper rotation	$\sigma_{\alpha\beta} = (\sigma_{yz}, \sigma_{zx}, \sigma_{xy})$
n	$\bar{n}$	$(0, 0, \sigma_{xy})$
$2'$	$m'\ (= \bar{2}')$	$(\sigma_{yz}, \sigma_{zx}, 0)$
$n'\ (\neq 2')$	$\bar{n}'\ (\neq m')$	(0,0,0)

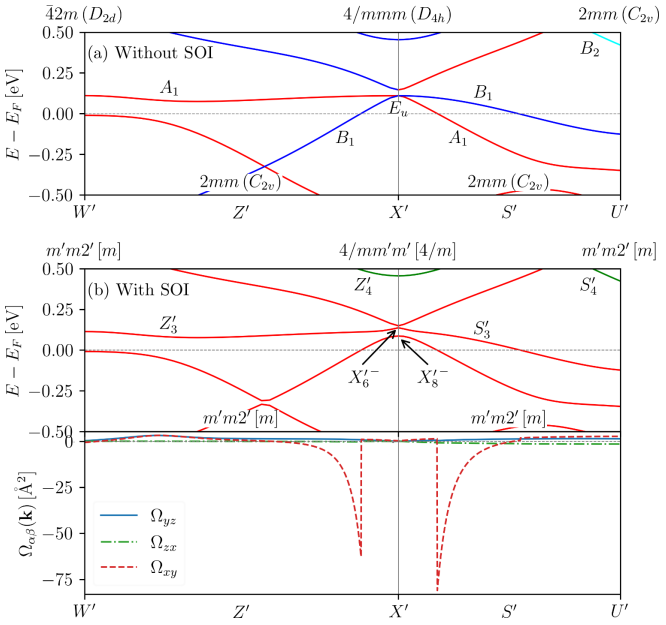

FIG. 6. Band structures and Berry curvatures along W'-X'-U' (a) without and (b) with SOI. The lifted essential degeneracy at X' due to SOI results in finite Berry curvatures. Berry curvature without SOI is not shown because it is negligibly small. The same conventions are adopted as in Fig. 3.

odd under TR, satisfies the constraint

$$\begin{pmatrix}\sigma_{yz}\\ \sigma_{zx}\\ \sigma_{xy}\end{pmatrix} = (-1)^s \det[R_{\mathbf{n}}(\theta)] R_{\mathbf{n}}(\theta) \begin{pmatrix}\sigma_{yz}\\ \sigma_{zx}\\ \sigma_{xy}\end{pmatrix}. \tag{A1}$$

$R_{\mathbf{n}}(\theta)$ is an orthogonal matrix, including both proper and improper rotations about an axis $\mathbf{n}$ by an angle θ. Determinant is there as AHC is a pseudovector; $s = 1$ with TR and $s = 0$ without TR.

For simplicity, we first consider a proper rotation about $\mathbf{n} = \hat{z}$. In this case, Eq. (A1) reduces to

$$\begin{pmatrix}\sigma_{yz}\\ \sigma_{zx}\\ \sigma_{xy}\end{pmatrix} = (-1)^s \begin{pmatrix}\cos\theta & -\sin\theta & 0\\ \sin\theta & \cos\theta & 0\\ 0 & 0 & 1\end{pmatrix} \begin{pmatrix}\sigma_{yz}\\ \sigma_{zx}\\ \sigma_{xy}\end{pmatrix}. \tag{A2}$$

By solving Eq. (A2), one finds that (i) if $s = 0$, only σ_{xy} can be nontrivial, (ii) if $s = 1$ and $\theta = \pi$, only σ_{yz} and σ_{zx} can be nontrivial, and (iii) if $s = 1$ and $\theta \neq \pi$, no nontrivial components exist. For an improper rotation, given as the product of a proper rotation and the inversion, one can easily show that the same conclusion holds. The discussion is summarized in Table II.

The symmetry constraints on Berry curvatures can be obtained similarly. In this case, we often find simple constraints along rotation-invariant axes or on mirror-invariant planes as a result of the $\mathbf{k}$ dependence of the Berry curvature.

APPENDIX B: BERRY CURVATURES AROUND X'

In Fig. 6, we show band structures and Berry curvatures along W'-X'-U'. Without SOI, there is one degenerate band that belongs to 2D irrep E_u of the little group $4/mmm\,(D_{4h})$ just above the Fermi energy at X'. After turning SOI on, the degeneracy is lifted into two 1D irreps X'^{-}_6 and X'^{-}_8 of the little group $4/mm'm'$. Berry curvatures become finite after the band belonging to X'^{-}_8 (Z'_3 and S'_3 to be exact) crosses the Fermi energy.

Notably, there is a band crossing between A_1 and B_1 below the Fermi energy in Fig. 6(a) which implies a nodal line in the $k_x = 0$ plane. However, no appreciable contribution around the gapped nodal line is observed in Fig. 6(b). Therefore, Berry curvatures around X' originate from the lifted essential degeneracy at X'.

[1] R. Karplus and J. M. Luttinger, Hall Effect in Ferromagnetics, Phys. Rev. **95**, 1154 (1954).

[2] N. Nagaosa, J. Sinova, S. Onoda, A. H. MacDonald, and N. P. Ong, Anomalous Hall effect, Rev. Mod. Phys. **82**, 1539 (2010).

[3] F. D. M. Haldane, Model for a Quantum Hall Effect without Landau Levels: Condensed-Matter Realization of the "Parity Anomaly", Phys. Rev. Lett. **61**, 2015 (1988).

[4] W. H. Kleiner, Space-time symmetry of transport coefficients, Phys. Rev. **142**, 318 (1966).

[5] M. Seemann, D. Ködderitzsch, S. Wimmer, and H. Ebert, Symmetry-imposed shape of linear response tensors, Phys. Rev. B **92**, 155138 (2015).

[6] H. Chen, Q. Niu, and A. H. MacDonald, Anomalous Hall Effect Arising from Noncollinear Antiferromagnetism, Phys. Rev. Lett. **112**, 017205 (2014).

[7] J. Kübler and C. Felser, Non-collinear antiferromagnets and the anomalous Hall effect, Europhys. Lett. **108**, 67001 (2014).

[8] S. Nakatsuji, N. Kiyohara, and T. Higo, Large anomalous Hall effect in a non-collinear antiferromagnet at room temperature, Nature (London) **527**, 212 (2015).

[9] A. K. Nayak, J. E. Fischer, Y. Sun, B. Yan, J. Karel, A. C. Komarek, C. Shekhar, N. Kumar, W. Schnelle, J. Kübler, C. Felser, and S. S. P. Parkin, Large anomalous Hall effect driven by a nonvanishing Berry curvature in the noncolinear antiferromagnet Mn_3Ge, Sci. Adv. **2**, e1501870 (2016).

[10] N. Kiyohara, T. Tomita, and S. Nakatsuji, Giant Anomalous Hall Effect in the Chiral Antiferromagnet Mn_3Ge, Phys. Rev. Appl. **5**, 064009 (2016).

[11] T. Suzuki, R. Chisnell, A. Devarakonda, Y. T. Liu, W. Feng, D. Xiao, J. W. Lynn, and J. G. Checkelsky, Large anomalous Hall effect in a half-Heusler antiferromagnet, Nat. Phys. **12**, 1119 (2016).

[12] Y. Zhang, Y. Sun, H. Yang, J. Železný, S. P. P. Parkin, C. Felser, and B. Yan, Strong anisotropic anomalous Hall effect and spin Hall effect in the chiral antiferromagnetic compounds Mn_3X (X = Ge, Sn, Ga, Ir, Rh, and Pt), Phys. Rev. B **95**, 075128 (2017).

[13] M.-T. Suzuki, T. Koretsune, M. Ochi, and R. Arita, Cluster multipole theory for anomalous Hall effect in antiferromagnets, Phys. Rev. B **95**, 094406 (2017).

[14] Z. Q. Liu, H. Chen, J. M. Wang, J. H. Liu, K. Wang, Z. X. Feng, H. Yan, X. R. Wang, C. B. Jiang, J. M. D. Coey, and A. H. MacDonald, Electrical switching of the topological anomalous

Hall effect in a non-collinear antiferromagnet above room temperature, Nat. Electron. **1**, 172 (2018).

[15] M. Kimata, H. Chen, K. Kondou, S. Sugimoto, P. K. Muduli, M. Ikhlas, Y. Omori, T. Tomita, A. H. MacDonald, S. Nakatsuji, and Y. Otani, Magnetic and magnetic inverse spin Hall effects in a non-collinear antiferromagnet, Nature (London) **565**, 627 (2019).

[16] L. Šmejkal, R. González-Hernández, T. Jungwirth, and J. Sinova, Crystal time-reversal symmetry breaking and spontaneous Hall effect in collinear antiferromagnets, Sci. Adv. **6**, eaaz8809 (2020).

[17] Z. Feng, X. Zhou, L. Šmejkal, L. Wu, Z. Zhu, H. Guo, R. González-Hernández, X. Wang, H. Yan, P. Qin, X. Zhang, H. Wu, H. Chen, Z. Xia, C. Jiang, M. Coey, J. Sinova, T. Jungwirth, and Z. Liu, Observation of the anomalous Hall effect in a collinear antiferromagnet, arXiv:2002.08712.

[18] W. Shi, L. Muechler, K. Manna, Y. Zhang, K. Koepernik, R. Car, J. van den Brink, C. Felser, and Y. Sun, Prediction of a magnetic Weyl semimetal without spin-orbit coupling and strong anomalous Hall effect in the Heusler compensated ferrimagnet Ti_2MnAl, Phys. Rev. B **97**, 060406(R) (2018).

[19] L. Šmejkal, A. H. MacDonald, J. Sinova, S. Nakatsuji, and T. Jungwirth, Anomalous Hall antiferromagnets, arXiv:2107.03321.

[20] S. Wurmehl, H. C. Kandpal, G. H. Fecher, and C. Felser, Valence electron rules for prediction of half-metallic compensated-ferrimagnetic behaviour of Heusler compounds with complete spin polarization, J. Phys.: Condens. Matter **18**, 6171 (2006).

[21] G. Y. Gao and K.-L. Yao, Antiferromagnetic half-metals, gapless half-metals, and spin gapless semiconductors: The $D0_3$-type Heusler alloys, Appl. Phys. Lett. **103**, 232409 (2013).

[22] M. E. Jamer, Y. J. Wang, G. M. Stephen, I. J. McDonald, A. J. Grutter, G. E. Sterbinsky, D. A. Arena, J. A. Borchers, B. J. Kirby, L. H. Lewis, B. Barbiellini, A. Bansil, and D. Heiman, Compensated Ferrimagnetism in the Zero-Moment Heusler Alloy Mn_3Al, Phys. Rev. Appl. **7**, 064036 (2017).

[23] A. P. Cracknell, Time-reversal degeneracy in the electronic band structure of a magnetic metal, J. Phys. C **2**, 1425 (1969).

[24] G. Burns and A. M. Glazer, *Space Groups for Solid State Scientists*, 3rd ed. (Academic Press, New York, 2013).

[25] C. J. Bradley and A. P. Cracknell, *The Mathematical Theory of Symmetry in Solids: Representation Theory for Point Groups and Space Groups* (Oxford University Press, New York, 1972).

[26] M. I. Aroyo, J. M. Perez-Mato, D. Orobengoa, E. Tasci, G. de la Flor, and A. Kirov, Crystallography online: Bilbao crystallographic server, Bulg. Chem. Commun. **43**, 183 (2011); https://www.cryst.ehu.es.

[27] M. I. Aroyo, J. M. Perez-Mato, C. Capillas, E. Kroumova, S. Ivantchev, G. Madariaga, A. Kirov, and H. Wondratschek, Bilbao crystallographic server: I. Database and crystallographic computing programs, Z. Kristallogr. Cryst. Mater. **221**, 15 (2006).

[28] M. I. Aroyo, A. Kirov, C. Capillas, J. M. Perez-Mato, and H. Wondratschek, Bilbao crystallographic server. II. Representations of crystallographic point groups and space groups, Acta Crystallogr. A **62**, 115 (2006).

[29] P. Giannozzi, S. Baroni, N. Bonini, M. Calandra, R. Car, C. Cavazzoni, D. Ceresoli, G. L. Chiarotti, M. Cococcioni, I. Dabo, A. D. Corso, S. de Gironcoli, S. Fabris, G. Fratesi, R. Gebauer, U. Gerstmann, C. Gougoussis, A. Kokalj, M. Lazzeri, L. Martin-Samos *et al.*, QUANTUM ESPRESSO: a modular and open-source software project for quantum simulations of materials, J. Phys.: Condens. Matter **21**, 395502 (2009).

[30] P Giannozzi, O. Andreussi, T. Brumme, O. Bunau, M. B. Nardelli, M. Calandra, R. Car, C. Cavazzoni, D. Ceresoli, M. Cococcioni, N. Colonna, I. Carnimeo, A. D. Corso, S. de Gironcoli, P. Delugas, R. A. DiStasio, A. Ferretti, A. Floris, G. Fratesi, G. Fugallo *et al.*, Advanced capabilities for materials modelling with QUANTUM ESPRESSO, J. Phys.: Condens. Matter **29**, 465901 (2017).

[31] J. P. Perdew, K. Burke, and M. Ernzerhof, Generalized Gradient Approximation Made Simple, Phys. Rev. Lett. **77**, 3865 (1996).

[32] P. E. Blöchl, Projector augmented-wave method, Phys. Rev. B **50**, 17953 (1994).

[33] A. Dal Corso, Pseudopotentials periodic table: From H to Pu, Comput. Mater. Sci. **95**, 337 (2014); https://dalcorso.github.io/pslibrary.

[34] H. J. Monkhorst and J. D. Pack, Special points for Brillouin-zone integrations, Phys. Rev. B **13**, 5188 (1976).

[35] G. Pizzi, V. Vitale, R. Arita, S. Blügel, F. Freimuth, G. Géranton, M. Gibertini, D. Gresch, C. Johnson, T. Koretsune, J. Ibañez-Azpiroz, H. Lee, J.-M. Lihm, D. Marchand, A. Marrazzo, Y. Mokrousov, J. I. Mustafa, Y. Nohara, Y. Nomura, L. Paulatto *et al.*, Wannier90 as a community code: new features and applications, J. Phys.: Condens. Matter **32**, 165902 (2020).

[36] S. S. Tsirkin, High performance Wannier interpolation of Berry curvature and related quantities with WannierBerri code, npj Comput. Mater. **7**, 33 (2021); https://wannier-berri.org.

[37] V. Heine, *Group Theory in Quantum Mechanics: An Introduction to its Present Usage* (Pergamon Press, New York, 1960).

[38] Bands are classified by the unitary subgroup of the little group (m for $m'm2'$ and $\bar{1}$ for $2'/m'$). This is allowable because the antiunitary symmetries in $I4/mm'm'$ do not lead to extra degeneracies [23]. See Ref. [25] for more thorough discussions.

[39] K. Manna, L. Muechler, T.-H. Kao, R. Stinshoff, Y. Zhang, J. Gooth, N. Kumar, G. Kreiner, K. Koepernik, R. Car, J. Kübler, G. H. Fecher, C. Shekhar, Y. Sun, and C. Felser, From Colossal to Zero: Controlling the Anomalous Hall Effect in Magnetic Heusler Compounds via Berry Curvature Design, Phys. Rev. X **8**, 041045 (2018).

[40] J. Noky, Q. Xu, C. Felser, and Y. Sun, Large anomalous Hall and Nernst effects from nodal line symmetry breaking in Fe_2MnX (X = P, As, Sb), Phys. Rev. B **99**, 165117 (2019).

[41] P. Li, J. Koo, W. Ning, J. Li, L. Miao, L. Min, Y. Zhu, Y. Wang, N. Alem, C.-X. Liu, Z. Mao, and B. Yan, Giant room temperature anomalous Hall effect and tunable topology in a ferromagnetic topological semimetal Co_2MnAl, Nat. Commun. **11**, 3476 (2020).

[42] S. Minami, F. Ishii, M. Hirayama, T. Nomoto, T. Koretsune, and R. Arita, Enhancement of the transverse thermoelectric conductivity originating from stationary points in nodal lines, Phys. Rev. B **102**, 205128 (2020).

[43] D. Xiao, Y. Yao, Z. Fang, and Q. Niu, Berry-Phase Effect in Anomalous Thermoelectric Transport, Phys. Rev. Lett. **97**, 026603 (2006).

[44] M. Kawamura, FermiSurfer: Fermi-surface viewer providing multiple representation schemes, Comput. Phys. Commun. **239**, 197 (2019); https://fermisurfer.osdn.jp.